Granular avalanches across irregular three-dimensional terrain: 2. Experimental tests

Richard M. Iverson, Matthew Logan, and Roger P. Denlinger
U.S. Geological Survey, Vancouver, Washington, USA

Received 29 August 2003; revised 21 January 2004; accepted 27 January 2004; published 27 March 2004.

[1] Scaling considerations indicate that miniature experiments can be used to test models of granular avalanches in which the effects of intergranular fluid and cohesion are negligible. To test predictions of a granular avalanche model described in a companion paper, we performed bench top experiments involving avalanches of dry sand across irregular basal topography that mimicked the complexity of natural terrain. The experiments employed a novel method of laser-assisted cartography to map the three-dimensional morphology of rapidly moving avalanches, thereby providing high-resolution data for comparison with model output. Model input consisted of two material properties (angles of internal and basal Coulomb friction of the sand), which were measured in independent tests, and of initial and boundary conditions that characterized the geometry of the experimental apparatus. Experimental results demonstrate that the model accurately predicts not only the gross behavior but also many details of avalanche motion, from initiation to deposition. We attribute this accuracy to a mathematical and computational formulation that conserves mass and momentum in three-dimensional physical space and satisfies the Coulomb equation in three-dimensional stress space. Our results support the hypothesis that a Coulomb proportionality between shear and normal stresses applies in moderately rapid granular flows and that complicated constitutive postulates are unnecessary if momentum conservation is strictly enforced in continuum avalanche models. Furthermore, predictions of our Coulomb continuum model contrast with those of a Coulomb point mass model, illustrating the importance of multidimensional modeling and model testing. *INDEX TERMS:* 3210 Mathematical Geophysics: Modeling; 1824 Hydrology: Geomorphology (1625); 1815 Hydrology: Erosion and sedimentation; 8020 Structural Geology: Mechanics; 8168 Tectonophysics: Stresses—general; *KEYWORDS:* avalanche, granular, experiments, landslide, model, three-dimensional

Citation: Iverson, R. M., M. Logan, and R. P. Denlinger (2004), Granular avalanches across irregular three-dimensional terrain: 2. Experimental tests, *J. Geophys. Res.*, *109*, F01015, doi:10.1029/2003JF000084.

1. Introduction

[2] Diverse mass movement phenomena, including rock avalanches, snow avalanches, debris flows, and pyroclastic flows, involve rapid downslope motion of deforming masses of solid grains and intergranular fluid. Ideal granular avalanches represent a limiting case, in which intergranular fluid and cohesion play negligible mechanical roles [e.g., *Savage and Hutter*, 1989, 1991]. Testing the ability of mathematical models to predict the behavior of ideal granular avalanches that move cross irregular topographic surfaces is a critical step toward understanding and predicting the behavior of rapid mass movements on the irregular surfaces of Earth and other planets.

[3] Although development of granular avalanche models is typically motivated by field applications, field data generally provide inconclusive model tests. Collection of detailed real-time data on full-scale natural avalanches is notoriously difficult and dangerous, and geological reconstructions of the behavior of bygone avalanches are too poorly constrained to provide decisive tests [e.g., *Voight et al.*, 1983]. Moreover, the variable influences of intergranular fluid and cohesion, unresolved geological heterogeneities, and uncontrolled initial and boundary conditions lead to considerable ambiguity about model performance because such influences bedevil efforts to distinguish whether prediction errors result from uncertain model input or from erroneous model formulation. Therefore geophysical applications of granular avalanche models should be preceded by tightly controlled laboratory experiments that provide unambiguous model tests [*Iverson*, 2003].

[4] In this paper we describe the design, execution, and results of novel laboratory experiments that tested predictions of a granular avalanche model presented in a companion paper [*Denlinger and Iverson*, 2004]. The central postulate of the model is that granular avalanches behave as isochoric flows of finite volumes of continuous media, in which mass and momentum are conserved and shear and normal stresses on internal and bounding surfaces obey the

Coulomb [1776] friction equation. To characterize the avalanche material, the model utilizes only two parameters: the quasi-static angles of internal friction and basal friction of the granular aggregate. Independent measurements of these parameters were part of our experiment protocol. Therefore our model predictions entailed no calibration, and our avalanche experiments provided stringent model tests.

[5] The avalanche experiments also served a purpose beyond model testing. Design of the experiments motivated a scaling analysis that helped clarify causes of scale-dependent behavior of geophysical avalanches. In addition, the need for high-resolution data motivated development of a new and economical method of laser-assisted analog cartography, which facilitated precise determination of the rapidly changing topography of avalanching masses. Similar methodology may prove useful not only in future avalanche experiments but also in other geomorphological experiments that require high-resolution mapping of topographic change.

2. Scaling and Experiment Design

[6] Scaling is a critical issue in the design of laboratory experiments intended to shed light on geophysical phenomena. The scaling analysis summarized below explains our rationale for employing miniature experiments with sand-air mixtures to test our granular avalanche model. On the other hand, the analysis also demonstrates that miniature experiments are unlikely to mimic some avalanche behavior that is possible at geophysical scales.

[7] Two scaling issues are especially pertinent: (1) Given that most granular avalanches involve some interaction of grains with fluid (e.g., air or water) and perhaps involve some intergranular cohesion, under what conditions are fluid and cohesion effects negligible? (2) Can the behavior of granular avalanches (with and without fluid and cohesion effects) be expected to vary with scale? We address these issues by deriving scaling parameters for an avalanche in which intergranular fluid properties and cohesion have arbitrary magnitudes. Evaluation of these parameters for diverse avalanche scenarios provides a basis for assessing the importance of fluid effects, cohesion effects, and the influence of avalanche scale.

[8] To identify relevant scaling parameters, we use the method of dimensional analysis, which assumes minimal a priori knowledge of avalanche dynamics. For the sake of brevity and clarity we restrict our analysis to a two-dimensional, fluid-filled granular avalanche descending a rigid, uniform slope, and we assume that the avalanche bulk density ρ is essentially uniform and that effects of the ambient fluid surrounding the avalanche are negligible (Figure 1). We also assume that the properties of the avalanche material do not change in transit (i.e., that grain fracture and comminution do not occur).

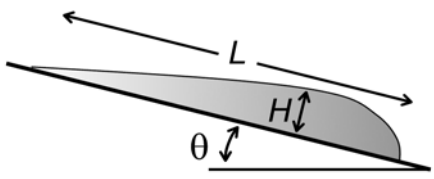

Figure 1. Schematic illustrating geometric quantities that characterize the cross-sectional geometry of a simplified two-dimensional granular avalanche descending a uniform slope. Vertical exaggeration is roughly 10 times.

Table 1. Variables Used in Dimensional Analysis of Avalanche Motion

Variable	Definition	Dimensions	Units
c	intergranular cohesion	M/LT^2	Pa
D	hydraulic diffusivity of grain-fluid mixture	L^2/T	$m^2\ s^{-1}$
e	restitution coefficient of colliding grains		
E	bulk compressive stiffness of granular mixture	M/LT^2	Pa
g	magnitude of gravitational acceleration	L/T^2	$m\ s^{-2}$
H	avalanche thickness	L	m
L	avalanche length	L	m
u	magnitude of avalanche velocity (speed)	L/T	$m\ s^{-1}$
δ	typical grain diameter	L	m
θ	bed slope		degrees
μ	dynamic viscosity of intergranular fluid	M/LT	Pa s
ρ	bulk density of granular mixture	M/L^3	$kg\ m^{-3}$
ρ_s	bulk density of solid grains	M/L^3	$kg\ m^{-3}$
ρ_f	bulk density of intergranular fluid	M/L^3	$kg\ m^{-3}$
τ	magnitude of avalanche stress	M/LT^2	Pa
ϕ_{int}	internal friction angle of granular mass		degrees
ϕ_{bed}	basal friction angle of grains contacting bed		degrees

[9] The first step in dimensional analysis involves positing a list of variables likely to influence the macroscopic dynamics of the avalanche as a whole, thereby ignoring some grain-scale variables considered by *Savage* [1984] and *Iverson* [1997]. Table 1 defines and categorizes a list of 17 pertinent variables, 13 of which are parameters that describe avalanche physical properties, 2 of which are lengths (H and L) that describe the avalanche size and shape, and 2 of which grossly characterize the dynamic response of the avalanche. These dynamic variables (the downslope avalanche velocity u and the typical avalanche stress τ) are posited to be functions of the other 15 variables, as represented symbolically by

$$(u, \tau) = f\left(g, L, H, \delta, \rho, \rho_s, \rho_f, D, \mu, \phi_{\text{int}}, \phi_{\text{bed}}, c, E, e, \theta\right). \quad (1)$$

Two additional independent variables that are likely important are not listed explicitly in equation (1) because they are specified implicitly through combinations of other variables: The intrinsic hydraulic permeability of the granular aggregate k is specified by $k = \mu D/E$, and the porosity of the granular aggregate n is specified by $n = (\rho - \rho_s)/(\rho_f - \rho_s)$.

[10] The second key step in our dimensional analysis involves selection of fundamental scales for mass, length, and time. In the case of fluid-filled granular avalanches, this selection is complicated by the existence of two important macroscopic length scales, H and L [cf. *Savage and Hutter*, 1989]. We address this complication below, but we first present a straightforward dimensional analysis that uses a single length scale, H. We consequently choose the mass scale as ρH^3 and the timescale as $\sqrt{H/g}$ because gravity and its effect on avalanche weight are the fundamental phenomena responsible for avalanche motion. By using these three scales and applying the Buckingham Π theorem and standard methods of dimensional analysis [e.g., *Logan*,

1987], equation (1) can be reduced to a functional relationship involving 14 dimensionless variables:

$$\left(\frac{u}{\sqrt{gH}},\frac{\tau}{\rho gH}\right) = f\left(\frac{L}{H},\frac{\delta}{H},\frac{\rho_s}{\rho},\frac{\rho_f}{\rho},\frac{D}{H^{3/2}g^{1/2}},\frac{\mu}{\rho H^{3/2}g^{1/2}},\frac{c}{\rho gH},\frac{E}{\rho gH},\phi_{\text{int}},\phi_{\text{bed}},e,\theta\right). \quad (2)$$

The dependent variables on the left-hand side of equation (2) are broadly indicative of avalanche dynamics and are readily identified as a normalized velocity or Froude number, $u/\sqrt{gH}$, and a normalized stress, $\tau/\rho gH$. According to equation (2), dynamic similarity should prevail in any two avalanches that each have the same values of all the independent variables on the right-hand side of the equation.

[11] The variables on the right-hand side of equation (2) can be grouped into categories with differing implications for similitude and scale modeling. The simplest category comprises the last four variables in equation (2), which are intrinsically dimensionless and are therefore expected to have identical effects at all scales. (For example, the friction angles ϕ_{int} and ϕ_{bed} characterize flow resistance that has the same effect on avalanches of any size.) A second category includes the first four variables on the right-hand side of equation (2), which are either simple density ratios or simple length ratios. The density ratios indicate no intrinsic scale dependence, and the length ratios indicate no scale dependence if geometric similarity is maintained (i.e., if L/H and δ/H are held constant). Identification of dynamic scale effects therefore focuses on the remaining four variables on the right-hand side of equation (2). Retaining only these variables reduces equation (2) to a listing of dynamic scaling parameters:

$$\left(\frac{u}{\sqrt{gH}},\frac{\tau}{\rho gH}\right) = f_{\text{scale}}\left(\frac{D}{H^{3/2}g^{1/2}},\frac{\mu}{\rho H^{3/2}g^{1/2}},\frac{c}{\rho gH},\frac{E}{\rho gH}\right). \quad (3)$$

Although equation (3) has clear relevance, the utility of the relationship can be enhanced by recognizing that the Froude velocity scaling $u \sim \sqrt{gH}$ is less important in granular avalanches than is the free-fall velocity scaling $u \sim \sqrt{gL}$ because the potential for free fall rather than the potential for wave translation generally governs motion on avalanche slopes, where inclinations commonly exceed 30° [*Savage and Hutter*, 1989; *Iverson*, 1997]. As a consequence, it is helpful to substitute the length scale L for the length scale H wherever the velocity scale $\sqrt{gH}$ occurs in equation (3). In addition, it is instructive to highlight the dependence of the hydraulic diffusivity D on the fluid viscosity μ by making the substitution $D = kE/\mu$ and to use the reciprocal of the second parameter on the right-hand side of equation (3). With these modifications, equation (3) becomes

$$\left(\frac{u}{\sqrt{gL}},\frac{\tau}{\rho gH}\right) = f_{\text{scale}}(N_P, N_R, c^*, E^*), \quad (4a)$$

where

$$N_P = \frac{\sqrt{L/g}}{\mu H^2/kE},\ N_R = \frac{\rho H\sqrt{gL}}{\mu},\ c^* = \frac{c}{\rho gH},\ E^* = \frac{E}{\rho gH}. \quad (4b)$$

The four scaling parameters listed in equation (4b) include two derived by *Iverson and Denlinger* [2001] by different means, and all have straightforward implications. The first parameter N_P can be viewed as a timescale ratio, in which $\sqrt{L/g}$ is the timescale for avalanche motion and $\mu H^2/kE$ is the timescale for diffusion of disequilibrium pore fluid pressure. Small values of N_P indicate a strong propensity for pore fluid pressure to influence avalanche motion. The second scaling parameter N_R is a type of Reynolds number, in which $\sqrt{gL}$ plays the role of the characteristic velocity. Small values of N_R indicate a strong propensity for fluid viscosity to influence avalanche motion. The third scaling parameter c^* is the intergranular cohesion normalized by the characteristic stress ρgH, and the fourth scaling parameter E^* is the bulk stiffness (reciprocal of compressibility) normalized by the same stress. Small values of c^* indicate little propensity for cohesion to affect avalanche motion, whereas small values of E^* indicate that bulk compression may significantly influence motion. Ideal granular avalanches may be defined as those in which effects of fluid pressure, viscosity, intergranular cohesion, and bulk compression are negligible; these conditions are satisfied when N_R, N_P, and E^* have large values (in principle, approaching ∞) and c^* has a small value (in principle, approaching zero).

2.1. Fluid Effects

[12] The parameters N_R and N_P provide a gauge of scale-dependent effects of pore fluid on avalanche motion. Figure 2 illustrates how values of these parameters vary as a function of fluid viscosity, avalanche permeability, and avalanche size (as measured by the characteristic thickness H). As avalanche size decreases, N_R values decrease, and the importance of viscous shear resistance (relative to inertia of the avalanche mixture) consequently increases. However, even miniature avalanches with $H \sim 0.01$ m are unlikely to exhibit significant viscous resistance if the pore fluid is air because N_R values exceed 10^6 in this instance (Figure 2). If the pore fluid is water, the situation is more ambiguous, and if the pore fluid is a muddy slurry (as in a debris flow), viscous effects may be quite significant at miniature scales ($H \sim 0.01$ m) but less significant at large scales ($H \sim 10$ m).

[13] As avalanche size decreases, values of N_P increase (opposite to the trend of N_R). Values of N_P exceed 10^5 if the avalanche thickness is small ($H \sim 0.01$ m), if the pore fluid is air, and if the granular aggregate is clean sand (Figure 2). Under these conditions, dissipation of nonequilibrium pore fluid pressures occurs very rapidly in comparison to the duration of avalanche motion, and pore pressure effects are likely to be negligible. Thus on the basis of N_P scaling and N_R scaling, small avalanches of dry clean sand in air satisfy the criteria for "ideal granular avalanches." The situation is less clear-cut with respect to large geophysical avalanches in which the pore fluid is air. If the avalanche thickness H reaches 10–100 m, N_R becomes very large but N_P decreases to ~1. Thus in such avalanches, nonequilibrium pore fluid pressure may persist once it is generated, and avalanche friction may be greatly reduced as a consequence [*Shreve*, 1968].

[14] The fact that N_R and N_P exhibit opposite trends as functions of avalanche size poses severe scaling problems if

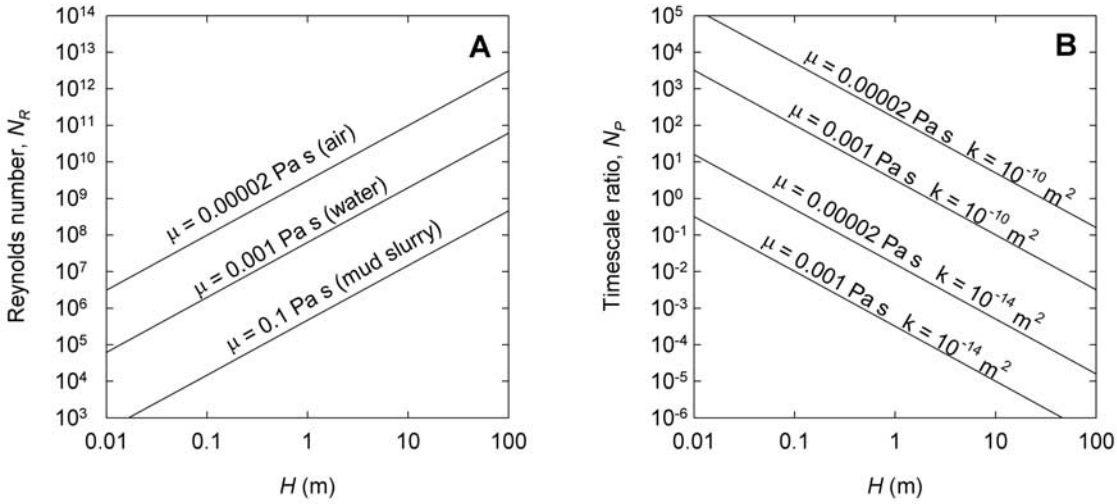

Figure 2. Graphs of the Reynolds number N_R and timescale ratio N_P as functions of avalanche size (as measured by thickness H) for values of fluid viscosity typical of air ($\mu = 0.00002$ Pa s), water ($\mu = 0.001$ Pa s), and mud slurry ($\mu = 0.1$ Pa s) and values of hydraulic permeability typical of clean sand ($k = 10^{-10}$ m^2) and poorly sorted debris with a muddy matrix ($k = 10^{-14}$ m^2). To generate these graphs, fixed values were assumed for three other quantities: the length-scale ratio $H/L = 100$ (typical of most avalanches), the compressive stiffness $E = 10^7$ Pa (typical of loose granular soils), and the bulk density $\rho = 1500$ kg m^{-3} (typical of loose granular soils) [cf. *Iverson and Denlinger*, 2001; *Iverson and Vallance*, 2001].

the pore fluid is at least as viscous as water. Figure 2 shows that viscous effects (as measured by N_R) are probably negligible in large geophysical avalanches containing water, whereas pore pressure effects (as measured by N_P) can be very significant. Nearly the opposite behavior is probable if water is present in a miniature, laboratory-scale avalanche, which is likely to exhibit significant viscous effects and little pore pressure effect. As a consequence, although ''ideal granular avalanches'' with negligible fluid effects are appropriate subjects for experimentation at miniature laboratory scales, experiments at much larger scales are necessary to investigate the dynamics of geophysical avalanches or flows with significant fluid effects [cf. *Iverson*, 1997; *Iverson and Denlinger*, 2001].

2.2. Solid Effects

[15] The parameters c^* and E^* provide a gauge of scale-dependent effects of grain interactions on avalanche motion, and Figure 3 illustrates how values of these parameters vary as functions of avalanche size, cohesive strength, and compressive stiffness. As indicated by Figure 3a, $E^* \gg 1$ generally applies in miniature, laboratory-scale avalanches of sand as well as in most geophysical avalanches. Thus scaling of compressive stiffness is not a major issue. On the

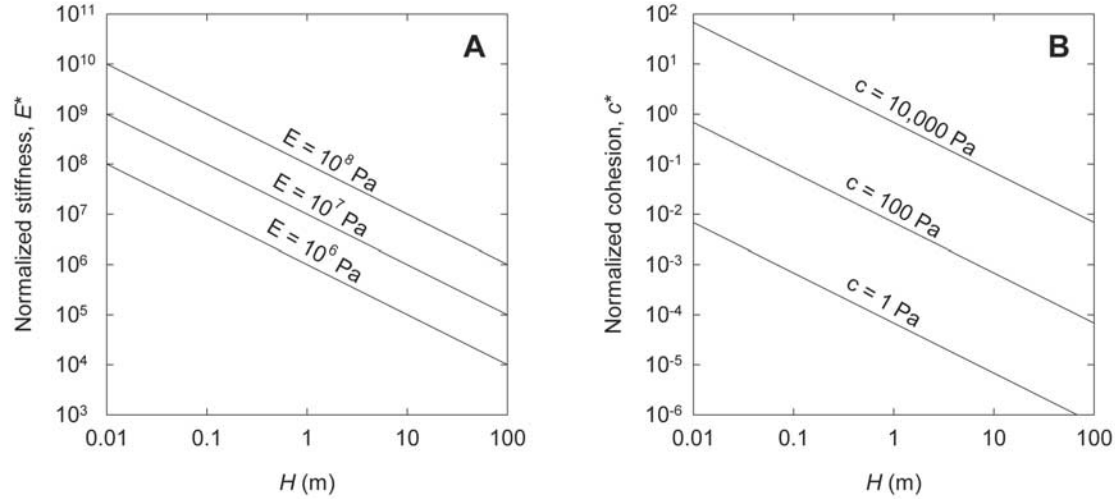

Figure 3. Graphs of the normalized stiffness E^* and normalized cohesion c^* as functions of avalanche size (as measured by thickness H) for values of cohesion c and compressive stiffness E typical of soils and fragmented rocks.

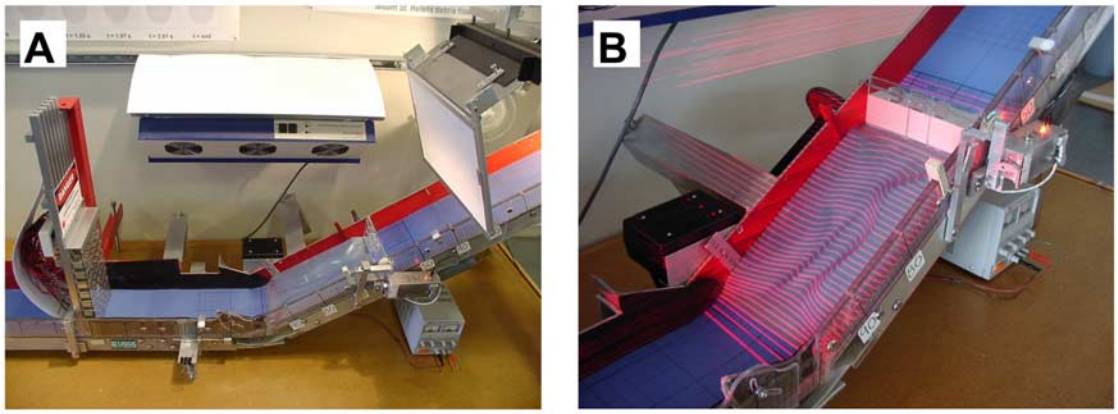

Figure 4. Oblique photographs of the miniature flume used in the avalanche experiments. (a) Entire apparatus (~1 m in length), with lasers mounted in the superstructure on the left, a white light diffuser (to aid photography) mounted on the right, and an ion emission hood (to neutralize electrostatic charges) mounted on the wall behind the flume. (b) Flume bed topography illuminated by superposed laser contours. Topography is in the "inverted" configuration of experiment B. White sand is loaded behind the flume head gate.

other hand, Figure 3b indicates that cohesive forces can potentially have a much greater effect in miniature avalanches than in full-scale avalanches, which generally have $c^* \ll 1$. Cohesive forces are undesirable in small-scale experiments intended to investigate ideal granular avalanches, and assessment of the origins and magnitudes of possible cohesive forces is therefore important.

[16] Cohesion is a somewhat imprecise term encompassing a variety of phenomena (other than gravity) that cause attraction of adjacent grains. In soils the most important cohesive forces derive from electrostatic effects, chemical bonding, and surface tension due to water menisci [*Mitchell*, 1976, p. 187–189]. In clay-rich soils, these forces can produce cohesions as large as tens of kPa, as depicted by the upper line in Figure 3b. On the other hand, dry granular soils and fragmented rocks are generally assumed to have negligible cohesion. Although this assumption is probably appropriate at large scales, even moderate cohesion can contaminate results of small-scale experiments intended to investigate ideal granular avalanches. Such cohesion is evident, for example, where electrostatic attraction causes grains of dust to adhere to vertical surfaces. Experience with dry granular materials flowing in chutes shows that electrostatic effects can cause irreproducible experimental results but that such effects can be minimized by using grains much larger than dust particles, by controlling environmental conditions such as relative humidity, and by grounding all surfaces in an attempt to equalize electrical potentials [cf. *Louge and Keast*, 2001].

[17] Measurements with an electrostatic voltmeter (Trek Inc. model 523-1-CE) (throughout, the use of trade names in this paper is for identification purposes only and does not constitute endorsement by the U.S. Geological Survey or the U.S. Government) indicate that static electrical potentials of various materials and surfaces in our laboratory commonly range from tens to thousands of volts relative to a local Earth-grounded state. Stationary sand exhibits little tendency to retain static charges (potentials are generally smaller than ±40 volts), but sand moving rapidly across our flume bed can generate persistent potentials of thousands of volts if no steps are taken to minimize this phenomenon.

[18] Estimates of tensile cohesion c (in Pa) due to electrostatic attraction can be obtained from a specialized form of Coulomb's law, $c = 4.4 \times 10^{-6} (V/d)^2$, where V is the magnitude of the electrical potential (in volts) across two surfaces separated by a distance d (in mm) [*Mitchell*, 1976, p. 188]. According to this equation, two surfaces separated by 1 mm and maintaining a potential of 5000 V will exhibit an attraction $c \sim 100$ Pa. Figure 3a indicates that cohesion of this magnitude is probably irrelevant in a field-scale avalanche with $H > 1$ m but may be large enough to significantly affect a miniature avalanche with $H \sim 0.01$ m. Therefore, although electrostatic effects are commonly neglected in granular avalanche experiments, it is wise to take all feasible precautions against development and/or persistence of electrostatic charges. Our precautions (described in section 3.2) included the use of an ion emission hood to neutralize static charges and the application of an antistatic agent on static-prone surfaces of our experimental apparatus.

3. Experimental Methods and Materials

[19] We used two types of flume experiments to test model predictions. We replicated each type of experiment several times and found that, provided we followed a strict protocol for minimizing electrostatic effects, data from replicate experiments were indistinguishable within the resolution of our measurements.

3.1. Flume Configuration

[20] The scaling considerations described in section 2 indicate that ideal granular avalanches can be investigated using miniature experiments, and we consequently conducted experiments in a bench top flume 0.2 m wide and ~1 m long (Figure 4). Sections of the flume upslope and downslope from the avalanche descent path were unchanged from a configuration used in previous avalanche

Table 2. Summary of Experiment Conditions and Sand Properties[a]

Conditions/Properties	Experiment A	Experiment B
Orientation of flume topography	"regular"	"inverted"
Aperture width of flume head gate, cm	12	4
Ambient relative humidity, %	36	66
Ambient temperature, °C	21	17
Shape of sand grains	angular	rounded
Diameter of sand grains, mm	0.5–1	0.25–0.5
Sand volume, cm^3	308	308
Sand mass, g	388.2	476.5
Sand bulk density, g cm^{-3}	1.26	1.55
Basal friction angle, sand on Formica, ϕ_{bed}, deg	23.47 ± 0.35	25.60 ± 0.77
Basal friction angle, sand on urethane, ϕ_{bed}, deg	19.85 ± 1.11	22.45 ± 0.66
Internal friction angle of sand, ϕ_{int}, deg	43.99 ± 0.29	39.39 ± 0.23

[a]Friction angles represent the mean ±1 standard deviation obtained from 10 tilt table measurements.

experiments without irregular topography [*Denlinger and Iverson*, 2001]. To add topography, the steep part of the flume (with slope averaging 31.6°) was fitted with a custom-formed urethane insert that provided an irregular basal surface. Rotation of the insert by 180° enabled experimentation with two distinct topographic configurations. Although these topographies exhibited many of the complexities of natural avalanche slopes, they were not intended to emulate any particular slope. Rather, they were designed to provide thorough tests of model predictions by promoting complicated and diverse avalanche behavior, including extending and compressing flow, divergence and convergence of flow around islands, superelevation of flow around curves, and stranding of static material.

[21] The head of the flume was fitted with a vertical glass head gate for suddenly releasing a static granular mass and initiating an avalanche (Figure 4b). The planar, sloping basal surface behind the head gate was lined with Formica, which also lined a planar, horizontal runout surface at the base of the flume. The vertical sidewalls of the flume were constructed of acrylic and aluminum. Both the head gate (in its closed position) and flume sidewalls formed rigid boundaries, across which no flux of grains occurred. Whereas many previous experiments have used en masse releases of granular avalanches with specified initial geometries [e.g., *Hutter and Koch*, 1991; *Wieland et al.*, 1999], our flume head gate had a restricted (and adjustable) aperture that caused some static sand to remain stranded upslope when the gate was opened [cf. *Denlinger and Iverson*, 2004]. As a consequence, the avalanche source area developed self-formed boundaries upslope of the head gate, analogous to the self-formed boundaries of natural avalanches and experimental avalanches with erodible beds [e.g., *McDonald and Anderson*, 1996]. The evolving transition between static and dynamic states in the sand upslope of the head gate served to severely test our model predictions because our theory and numerical methods were optimized for computing avalanche dynamics, not static stresses in stationary sand [*Denlinger and Iverson*, 2004].

3.2. Material Properties and Protocols

[22] The granular materials used in our experiments were two quartz sands with properties summarized in Table 2. We employed these sands owing to their homogeneity, relatively high density, and relatively inert chemical and electrical state (and because preliminary tests with several candidate materials showed that homogeneous quartz sands provided the best reproducibility of friction angle measurements). Prior to use we oven-dried and sieved the sands so as to retain only grains with diameters nominally ranging from 0.5 to 1 mm in the case of sand A and from 0.25 to 0.5 mm in the case of sand B. Another difference between the two sands involved grain roughness. Sand A consisted of angular, high-sphericity grains, whereas sand B consisted of well-rounded, moderately spherical grains (Figure 5).

[23] Quasi-static measurements of the friction angles of the two sands were made using a tilt table apparatus, pictured in Figure 6. The apparatus was fitted with three test platens, one of which was composed of urethane identical to that of the irregularly sloping bed of the flume. Another platen was composed of Formica identical to that of the planar bed surfaces behind the head gate and at the base of the flume, and the third platen was lined with very coarse sandpaper that inhibited basal slip. The procedure in each friction angle measurement consisted of first placing on each test platen horizontal tabular prisms of sand 240 mm long and 85 mm wide. For both sands the prism thickness was 6 mm on the sandpaper platen, whereas the prism thickness on the urethane and Formica platens was 1 mm

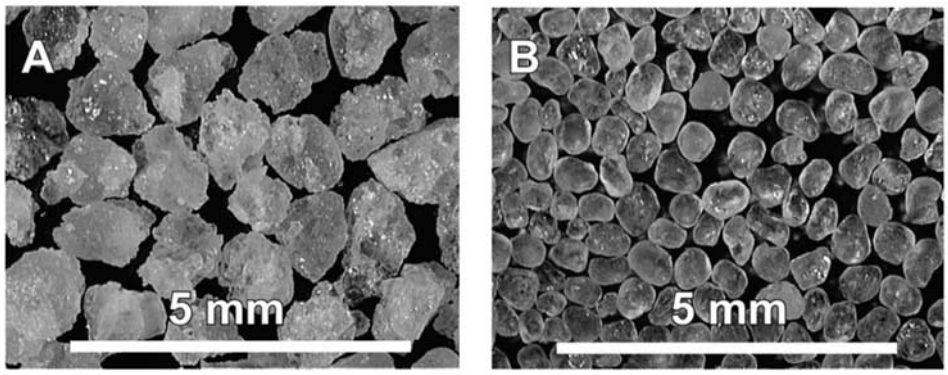

Figure 5. Photomicrographs of the two quartz sands used in flume experiments. (a) Angular grains, 0.5–1 mm diameter. (b) Rounded grains, 0.25–0.5 mm diameter.

Figure 6. Photograph of the tilt table apparatus used to make friction angle measurements. White sand is loaded on the three test platens. A digital inclinometer rests on the table top.

in the case of sand A and 2 mm in the case of sand B. A motor-driven worm gear was used to slowly increase the inclination of the tilt table until widespread slippage of one or more of the sand prisms was observed. Tilting was then stopped, and the angle at which slippage occurred was measured with a digital inclinometer (with precision $\pm 0.1^\circ$). Tilting was then continued until slippage of all three prisms was complete. Observations confirmed that sand slipped preferentially along the urethane and Formica test platens (thereby providing data on ϕ_{bed}) but sheared internally above the sandpaper surface (thereby providing data on ϕ_{int}). Table 2 summarizes results of the friction angle measurements as well as other experimental variables.

[24] To reduce data contamination due to electrostatic effects, we conducted all friction angle measurements and avalanche experiments under an ion emission hood (Electrostatics model HM-8000) to neutralize surface charges, and we conducted all friction angle measurements immediately prior to avalanche experiments and under a limited range of relative humidities (30–70%). We also found that reproducibility was best if we applied an antistatic aerosol (Staticguard) to the urethane test platen and flume bed a day or two prior to conducting experiments, and this application was adopted as part of our standard protocol.

[25] The protocol for avalanche experiments included several steps in addition to the antistatic precautions described above. In each experiment, 308 cm^3 of sand was placed behind the flume head gate by slowly pouring it from a graduated cylinder. The sand volume before and after pouring remained essentially constant, and no attempt was made to modify the packing of the sand behind the head gate. We therefore assumed that the sand retained a loose packing and bulk density similar to that inferred from weighing the sand-filled cylinder (Table 2). The surface of the sand behind the head gate was manually graded to form a right triangular prism with a horizontal upper surface and with the following dimensions: 4.35 cm vertical height (against the head gate), 7.07 cm horizontal length, and 20 cm horizontal width. The head gate aperture varied from 12 to 4 cm between experiments (Table 2), and in each experiment the gate was opened almost instantaneously by a spring-loaded release mechanism, which also activated an electronic analog timer that displayed the time elapsed since gate opening commenced.

3.3. Digital Photography and Laser Cartography

[26] The basic data acquired in our avalanche experiments consisted of sequential snapshots of the avalanche geometry recorded in vertical photographs obtained with an Olympus E-100 RS digital camera mounted ~2 m above the flume. In these 1.4 megapixel photographs the spatial resolution was ~0.46 mm on the flume bed, the nominal exposure time was 0.025 s, and the nominal interval between successive frames was 0.2 s. Precise time stamping of each photo frame with a resolution of 0.01 s was accomplished by including the electronic analog timer in the field of view of the camera.

[27] The rapidly changing three-dimensional geometry of avalanching masses was mapped using a novel cartographic technique, in which horizontal sheets of light from 52 refracted laser beams were used to superpose topographic contours at 5 mm intervals on the flume bed and moving avalanche surfaces. (This technique was a more precise hybrid of laser sheet and shadow bar techniques described previously by *McDonald and Anderson* [1996], *Denlinger and Iverson* [2001], and *Pouliquen and Forterre* [2002].) To produce contours, the 52 laser modules were mounted in a specially fabricated superstructure that enabled precise adjustment of the elevation and orientation of individual laser beams (Figure 4). Each beam was passed through a vertically oriented cylindrical lens (i.e., a 4 mm diameter glass rod) that refracted the beam into a horizontal sheet. Illuminated contours appeared where the laser sheets intersected the flume bed or avalanche surface. Table 3 summarizes the technical specifications of the lasers.

[28] Sequences of rectified vertical digital photographs were used to record each experiment. Rectification was necessary to correct for the effects of lens-dependent distortion and foreshortening that are inherent features of two-dimensional photographs of three-dimensional objects. Our rectification procedure employed a reference photograph of the bare flume bed and standard image-editing software. The reference photograph was digitally dissected into small quadrilateral blocks, which were reassembled to fit on an undistorted square grid by digitally ''stretching'' the blocks to relocate the vertices of each quadrilateral. Relocation coordinates necessary to fit the bare bed photograph to a regular grid were recorded within the image-editing software, and the same corrections were then applied to each photograph of the avalanche. This

Table 3. Properties of Laser Diode Modules

Property	Value or Class
Diode composition	AlGaInP (aluminum gallium indium phosphate)
Operating voltage, V DC	3–6
Operating power, mW	~2 (class IIIa laser)
Wavelength, nm	560 ± 10
Aperture diameter, mm	3
Divergence, mrd	<2
Optics	aspherical plastic collimating lens
Case material	copper

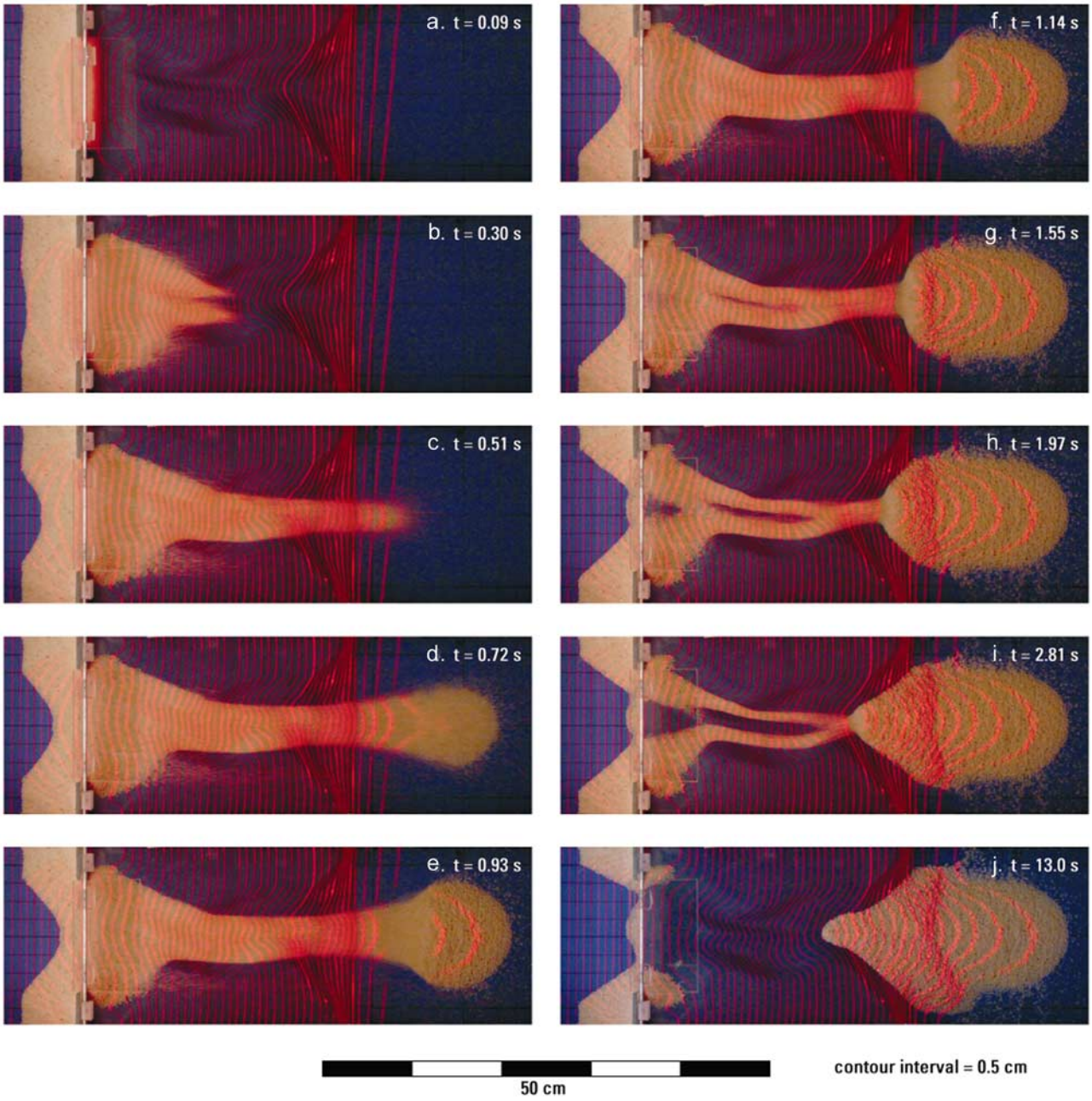

Figure 7. Sequence of vertical orthophotographs depicting avalanche experiment A. Timestamps express the time elapsed since the opening of the head gate at $t = 0$. Figure 7j shows the avalanche deposit after all motion has ceased. Table 2 summarizes properties of the avalanche sand (white) and flume bed (dark blue). Table 3 summarizes properties of the lasers used to project topographic contours (pink) at 5 mm intervals.

method of rectification produced nearly acceptable orthophotographs, but it did not correct for parallax errors that were most pronounced where large sand depths occurred near the edges of a photograph. The largest of these parallax errors produced fictitious longitudinal displacements of ~6.5 mm where sand was piled vertically against the flume head gate and fictitious lateral displacements of ~3 mm where sand was piled vertically against the flume sidewalls behind the head gate. These errors were removed during data processing by employing sand thicknesses that conformed with the known geometry of the static sand behind the head gate.

3.4. Data Processing

[29] Additional data processing was necessary to produce a series of avalanche isopach maps suitable for comparison with numerical predictions of the vertical avalanche thickness $h(x, y, t)$, where x and y are planimetric map coordinates and where t is time. First, the planimetric positions of each topographic contour on the rectified photographs were

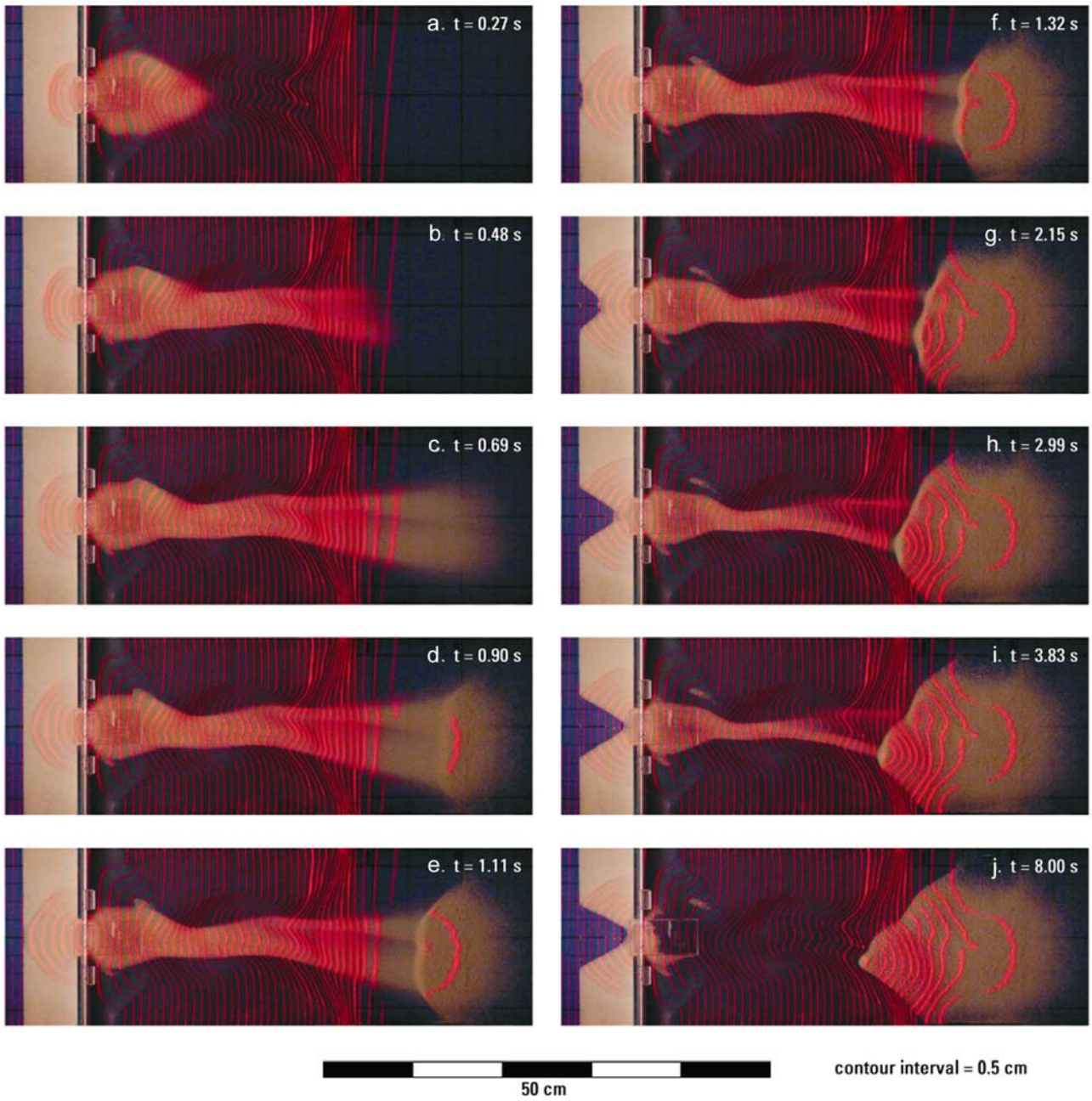

Figure 8. Same as Figure 7, but for experiment B.

digitized at an interval equivalent to ~3 mm on the flume bed. The three-dimensional coordinates of the digitized contours were then interpolated using a Kriging algorithm to produce mathematical surfaces representing the bare flume bed and avalanche surfaces. The flume bed surface was then subtracted from the avalanche surface to obtain $h(x, y)$, and this quantity was contoured to yield an isopach map. The net result of these procedures was the production of avalanche isopach maps with calculated horizontal errors smaller than 3 mm longitudinally and 1.5 mm laterally and with calculated vertical errors smaller than 0.5 mm.

4. Results

[30] Figures 7 and 8 depict key frames in the sequences of rectified vertical photographs of each avalanche experiment, and Figures 9 and 10 depict isopach maps that compare the results of the avalanche experiments with predictions of our computational model [*Denlinger and Iverson*, 2004]. The experimental data plotted in Figures 9 and 10 are also available in tabular form[1].

4.1. Observations of Avalanche Behavior

[31] Inspection of the photographs in Figures 7 and 8 reveals some important features of avalanche behavior. Most conspicuous is a great variation of avalanche width and cross section in both time and space, which gives the avalanches a strongly three-dimensional character. However,

[1] Auxiliary material is available at ftp://ftp.agu.org/apend/jf/2003JF000084.

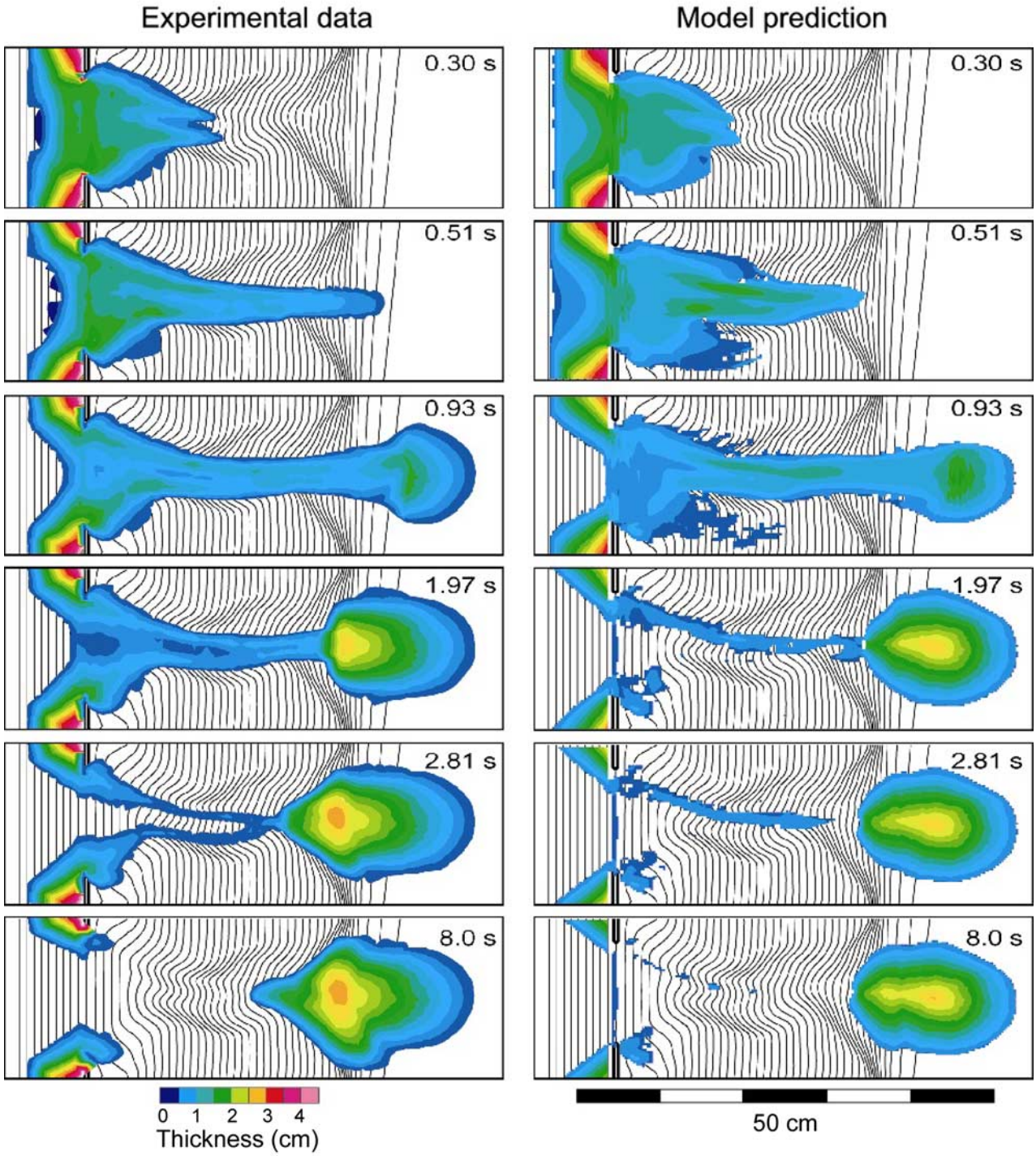

Figure 9. Isopach maps of vertical avalanche thickness h, comparing data and model predictions for experiment A. Isopachs are plotted on a topographic base with a contour interval of 5 mm.

despite this variation and variations in sand properties, the maximum speeds and runout distances of the two avalanches are similar. The observed maximum speeds ($u \sim 1$ m s^{-1}), taken in combination with the observed avalanche lengths ($L \sim 0.5$ m), yield a nondimensional avalanche speed $u/\sqrt{gL} \sim 0.4$–0.5 in each experiment. This nondimensional speed implies a maximum speed of 40–50 m s^{-1} in a dynamically similar geophysical avalanche with $L = 1$ km. Such speeds appear to be relatively common in natural rock and snow avalanches [*Voight*, 1978], indicating that the gross dynamic behavior of the experimental avalanches is indeed similar to that of geophysical prototypes.

[32] Perhaps the biggest mechanical difference between natural avalanches and the experimental avalanches depicted in Figures 7 and 8 results from the regulated release of sand from the flume head gate. The release is

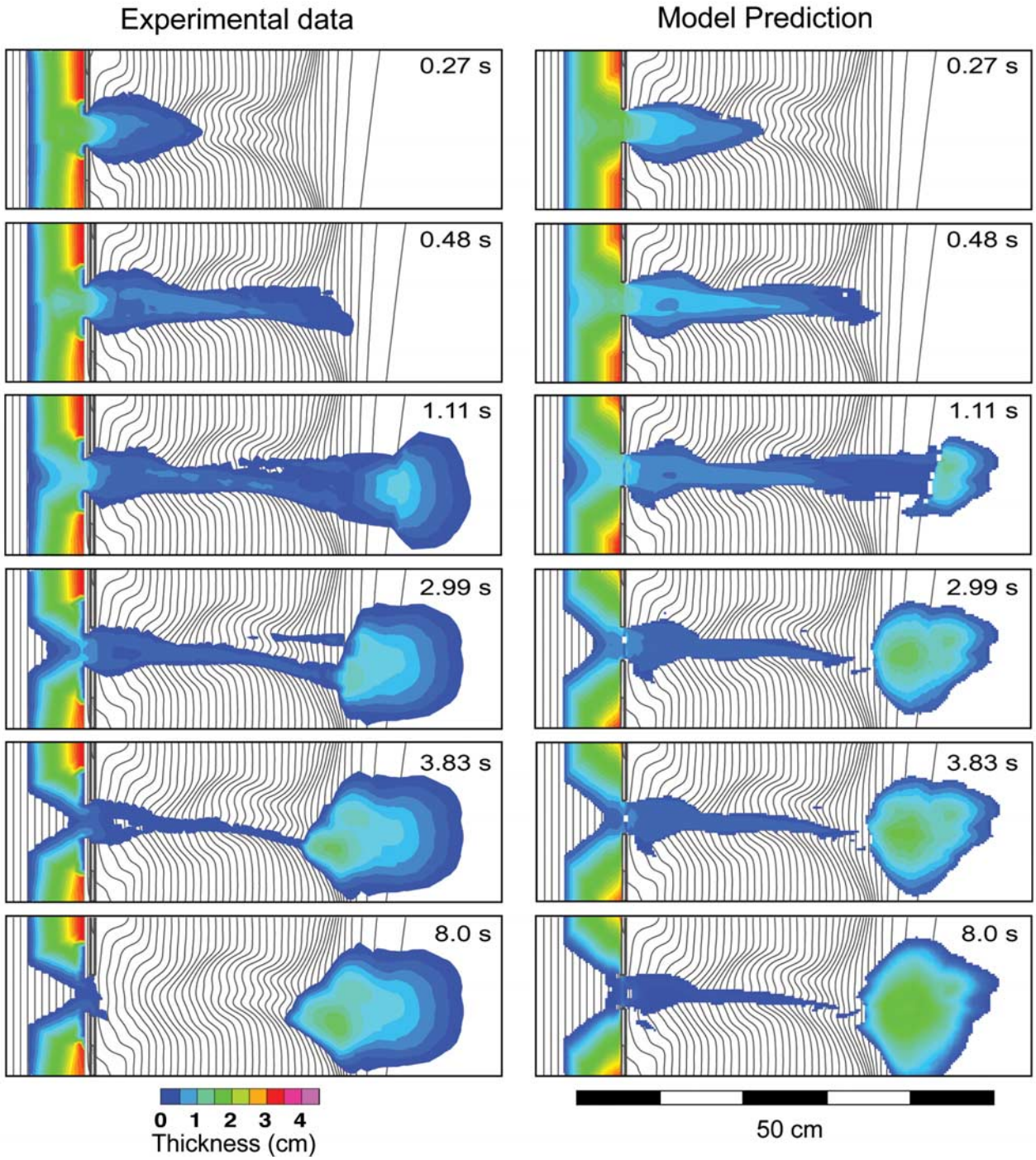

Figure 10. Same as Figure 9, but for experiment B.

probably more gradual, and perhaps more complicated, than a typical natural avalanche release, but these aspects of the experimental release facilitate model testing. When the head gate opens, sand initially collapses off a vertical free face and then begins to evacuate an amphitheater-shaped depression that forms upslope of the head gate (e.g., Figures 7a and 8a). The margin of the growing depression propagates upslope and laterally at a finite speed, and a distinct boundary separates the moving sand in the depression from the adjacent stationary sand. Eventually, the growing depression intersects the upper margin of the sand prism, but thereafter, sand continues to collapse laterally into a widening chasm, which develops a distinct V shape in both cross section and plan view. The nearly planar facets that bound the V notch continue to retreat laterally while maintaining a surface slope of $\sim 30^\circ$, intermediate between the sands' angles of basal and internal friction. In experiment A (with a 12-cm-wide head gate) the V notch ultimately enlarges to form a trapezoidal notch (e.g., Figure 7g). At the conclusion of each experiment the static sand left stranded upslope of the head gate retains the nearly planar facets that bounded the growing notch.

[33] In each experiment, some additional stranding of sand results from the presence of a slight topographic step, or lip, immediately beneath the aperture of the head gate. This upslope-facing step is formed by the upper edge of the urethane insert that provides three-dimensional bed topography. The step is ~0.2 mm in height normal to the bed and is too subtle to be depicted by the 5 mm contours in Figures 7 and 8. However, the step is represented mathematically in the bed configurations used in our computational model [*Denlinger and Iverson*, 2004].

[34] Comparison of Figures 7 and 8 indicates that the deposits at the foot of the two avalanche slopes have strong similarities but also clear differences that reflect differences in sand properties, bed topography, and avalanche dynamics. The distal margins of both deposits are emplaced almost entirely by the leading edges of the avalanches, and the trailing sand shows little tendency to override the distal deposits or push them forward (corroborating observations of *Davies and McSaveney* [1999]). The distal margin of the deposit in experiment B is relatively diffuse, a consequence of a relatively strong tendency for the spherical sand in this avalanche to saltate.

[35] In each experiment a migrating shock front separates the already emplaced static sand in the deposit from the rapidly flowing sand that impinges on the rear of the deposit [cf. *McDonald and Anderson*, 1996; *Gray et al.*, 2003]. The shock front is particularly visible in Figures 8e–8i, where it appears as a light-toned band that lacks superposed contour lines owing to its upstream-facing aspect. The final, static deposits of each avalanche consist of two parts: a distal lobe with a relatively flat surface, emplaced en masse during the initial surge prior to shock development, and a relatively steep proximal "talus slope" accreted at the shock front. In each deposit, subtle lateral wings form late in the depositional process by deflection of some sand that impinges against the growing talus slope. In Figure 7 (experiment A) the distal lobe, proximal talus slope, and lateral wings of the deposit are quite symmetrical axially, reflecting the dominance of downslope momentum as sand descends the lower part of the slope. In Figure 8 (experiment B), all features of the deposit are less symmetrical, reflecting diversion of the avalanche into two distinct sand streams by topography near the base of the slope. The deposit of experiment B also features two overlapping talus cones and a medial ridge that form by interaction of these streams.

4.2. Quantitative Model Tests

[36] Figures 9 and 10 depict isopach maps that compare the results of the avalanche experiments with predictions of our computational model [*Denlinger and Iverson*, 2004]. In model predictions, any sand thickness $h \geq 0$ is feasible owing to the continuum representation of h, but thicknesses smaller than ~0.5 mm have little physical meaning in the context of our experiments, wherein 0.5 mm is the diameter of a typical sand grain. Therefore as a basis for comparison with experimental data, model predictions shown in Figures 9 and 10 place avalanche margins where the predicted vertical sand thickness satisfies $h(x, y, t) = 0.5$ mm, and smaller thicknesses are omitted. In experiments, localized regions where the spatially averaged avalanche thickness is less than one grain diameter can occur due to saltation of dispersed grains (e.g., as is visible to the right of the main avalanche path in Figures 7b–7f). However, our mathematical model does not represent the physics of saltation, and we therefore omit regions of "apparent saltation" from model predictions.

[37] Figure 9 shows that model predictions match many of the details as well as the overall behavior of the avalanche in experiment A. Errors in prediction of the avalanche front speed are <15% at all times, and errors in prediction of the distal limit of the avalanche deposit are ~3%. The effects of topographic forcing on the three-dimensional form and lateral limits of the avalanche are predicted well, especially during the first ~1 s of avalanche motion and deposition. The predicted form of the final avalanche deposit is slightly more rotund than that of the experimental deposit, but the predicted deposit exhibits the same two-part morphology (with a distal lobe and proximal talus slope) evident in the experimental data.

[38] In Figure 9 the form and slope of the facets in sand stranded upslope of the head gate are quite similar in the predictions and data. This similarity is noteworthy because formation of the facets involves a strongly three-dimensional interplay of basal and internal Coulomb friction, and we interpret this similarity as evidence in support of our methodology for stress state computation [*Denlinger and Iverson*, 2004]. As shown in the last few panels of Figure 9, the model predicts a continuing trickle of thin sheets of sand off these facets after motion has ceased in the experiment. The trickle originates at the acute, three-dimensional corner formed by the sand facets and the edge of the head gate adjacent to the aperture. The trickle results from computational errors that accrue at this corner due to difficulties in balancing fluxes across nonorthogonal faces not represented in our computational grid. Adaptive mesh refinement may provide a remedy [cf. *LeVeque*, 2002], although we have not yet explored this approach.

[39] Figure 10 shows that model predictions for experiment B are, in most respects, as good or better than predictions for experiment A. The similarity of the observed and computed avalanche forms in the first two panels of Figure 10 ($t = 0.27$ s and 0.48 s, respectively) is particularly striking. At $t \geq 0.90$ s, differences in the geometry of observed and computed deposits result largely from dispersal of the distal margin due to sand saltation in the experiments. Model predictions of the growth and form of the V notch upslope from the head gate in this experiment illustrate that convergence of sand toward the narrow gate aperture causes a slower discharge (and slower V notch growth) than in experiment A.

5. Discussion

[40] The predictive accuracy evident in Figures 9 and 10 was attained by making several major improvements in a multidimensional continuum model described previously [*Iverson and Denlinger*, 2001; *Denlinger and Iverson*, 2001]. In section 5.1 we emphasize two of these improvements, which are particularly noteworthy because they involve improved representations of fundamental mechanics [*Denlinger and Iverson*, 2004]. To facilitate discussion of additional mechanical issues, we also contrast the predic-

tions of our improved avalanche model with those of a much simpler point mass model.

5.1. Improved Representation of Mechanics

[41] One major improvement in our model entailed the use of a new formulation for conserving momentum and estimating the effects of vertical accelerations on basal and internal stresses. The presence of vertical accelerations is a source of concern in all depth-averaged flow models, which commonly assume no vertical momentum component [e.g., *Vreugdenhil*, 1994], but vertical accelerations are particularly crucial in Coulomb avalanche models owing to the presence of steep slopes (>30°) and the effect of normal stresses on shear resistance. Previous depth-averaged models of multidimensional Coulomb avalanches incorporate the effects of vertical accelerations through the use of curvilinear coordinate systems, in which the x and y axes, for example, are fitted to basal topography [e.g., *Gray et al.*, 1999; *Iverson and Denlinger*, 2001]. Then, a combination of slope-parallel accelerations and centripetal accelerations associated with bed curvature combine to represent vertical acceleration effects. However, in fitted-coordinate models such as those of *Gray et al.* [1999] and *Iverson and Denlinger* [2001], bed curvature in the x direction has no effect on Coulomb reaction stresses that affect motion in the y direction and vice versa, a mathematical artifact that does not faithfully represent the pertinent physics. We therefore adopted a new approach, in which a rectangular Cartesian coordinate system is employed and effects of vertical accelerations on all stress components are computed explicitly. *Denlinger and Iverson* [2004] describe the mathematical details of our new approach and illustrate how vertical acceleration affects computational accuracy.

[42] Another major model improvement entailed the representation of Coulomb stress states in three dimensions. Prior approaches represented Coulomb stresses on planes normal to the bed in terms of depth-integrated lateral Earth pressure coefficients derived from two-dimensional Rankine state theory [e.g., *Savage and Hutter*, 1989, 1991; *Hutter and Koch*, 1991; *Gray et al.*, 1999; *Iverson and Denlinger*, 2001]. These coefficients assumed one of several discrete values, which depended only on whether the granular mass was locally extending or compressing as it moved downslope. In our new approach we retain the use of depth-integrated lateral stress coefficients, but these coefficients can assume any value consistent with a depth-averaged three-dimensional Coulomb stress state. Shear stresses on arbitrarily oriented planes arise naturally in this approach and are included in momentum balance calculations. *Denlinger and Iverson* [2004] describe the mathematical and computational details of our Coulomb calculations, which yield smoother stress distributions than those attained with previous approaches.

[43] The accuracy of our model predictions lends support to the *Savage and Hutter* [1989] hypothesis that a simple Coulomb proportionality ($\tau = \sigma \tan \phi$) between shear stress τ and normal stress σ is a robust feature of granular avalanches. This finding may seem surprising given that the relatively high speed ($u \sim 1$ m s^{-1}) and small thickness ($H \sim 5$ mm) of our experimental avalanches imply depth-averaged shear rates $u/H \sim 200$ s^{-1} if a no-slip basal boundary condition is assumed. Such shear rates are considerably larger than shear rates that may be typical of most geophysical avalanches [*Iverson and Vallance*, 2001] and are far larger than the shear rates that characterize classical quasi-static Coulomb behavior.

[44] Three important considerations indicate that Coulomb behavior in our avalanches is, in fact, unsurprising. First, our avalanches exhibited a large amount of basal slip, rendering internal shear rates less (perhaps much less) than the depth-averaged estimate of 200 s^{-1}. A large amount of basal slip is understandable because internal friction angles exceeded basal friction angles by factors of roughly 2 (Table 2). Second, an appropriate nondimensional characterization of the effect of avalanche shear rates on intergranular stress generation, the Savage number, indicates that conditions in our experimental avalanches were not far from the regime in which grain interactions are dominated by enduring, frictional contacts. For conditions in our avalanches the Savage number can be approximated as [*Iverson and Denlinger*, 2001]

$$N_S \approx \frac{u^2 \delta^2}{g H^3}. \tag{5}$$

Assuming no basal slip and inserting applicable values in equation (5) ($u = 1$ m s^{-1}, $\delta = 0.0005$ m, $g = 9.8$ m s^{-2}, $H = 0.005$ m) yields $N_S \approx 0.2$. *Savage and Hutter* [1989] observed that the transition from friction-dominated to collision-dominated granular flow occurs when N_S exceeds ~0.1. Thus if our avalanches were "collisional," they were only moderately so. More likely, the applicable Savage number for our avalanches was smaller than 0.1 owing to basal slip and consequent reduction of the internal shear rate, and our avalanches were mostly frictional.

[45] The third reason Coulomb behavior is not surprising is that granular materials generally exhibit a Coulomb-like proportionality between shear and normal stresses even when they are fully fluidized and undergo collisional flow. The ubiquity of this proportionality was the central finding of the seminal experiments of *Bagnold* [1954], which has been reinforced by subsequent work [*Hunt et al.*, 2002]. In shallow flows with free upper surfaces (as occur in our avalanches), normal stresses on planes parallel to the surface adjust freely to balance the weight of the superincumbent granular mass (plus departures from the static weight due to vertical accelerations). In deforming regions, shear stresses adjust to normal stresses accordingly. Thus to a substantial degree, all stresses depend ultimately on the bulk weight and inertia of the granular aggregate, irrespective of the shear rate. The success of our computational model hinges partly on the robustness of this phenomenon.

[46] The prevalence of Coulomb behavior in granular avalanches can be viewed as a consequence of self-organization and feedback. Mechanical interactions at innumerable grain contacts give rise to relatively predictable macroscopic stresses in homogeneous granular masses that deform inertially on a continuum scale because stresses continually adjust to balance the effects of momentum fluxes. The Coulomb equation appears to provide a good summary of this behavior as it yields accurate predictions

when used in conjunction with accurate accounting for macroscopic momentum conservation.

5.2. Comparison With a Point Mass Model

[47] To further assess quasi three-dimensional Coulomb behavior, it is useful to compare our model results (Figures 9 and 10) with results of the simplest possible Coulomb model, the sliding point mass model introduced by *Heim* [1932]. This model assumes that avalanche motion is described by the one-dimensional momentum conservation equation

$$d^2p/dt^2 = du/dt = g(\sin\theta - \cos\theta \tan\phi_{bed}), \qquad (6)$$

where p is avalanche position measured along the ground surface, u is downslope avalanche velocity parallel to the surface, t is time, g is the magnitude of gravitational acceleration, θ is the slope angle, and ϕ_{bed} is the angle of friction for basal sliding. *Heim*'s [1932] model omits many effects of multidimensional mass and momentum conservation, but it contains an elementary representation of gravity-driven sliding resisted by Coulomb friction, which forms the kernel of Coulomb avalanche models [cf. *Savage and Hutter*, 1989, 1991; *Iverson and Denlinger*, 2001]. Integrating equation (6) along an avalanche path, neglecting centripetal acceleration effects due to path curvature (as is tacitly assumed in equation (6)), and applying suitable initial conditions yields the famous *Heim* [1932] equation for the relationship between the vertical descent D and horizontal reach R of the avalanche, $D/R = \tan\phi_{bed}$. (Generally, H/L is used in this equation rather than D/R, which is used here to avoid confusion with our prior usage of H and L.)

[48] The integration of equation (6) that yields the *Heim* [1932] equation also yields predictions of avalanche position at all times. Figure 11 compares these predictions with the position of the avalanche front observed in experiments A and B and with predictions of our multidimensional continuum model. (Note that results depicted in Figure 11 cannot be extracted directly from Figures 9 and 10 without performing coordinate transformations; Figures 9 and 10 depict planimetric projections of the avalanche slope, not distance along the slope as employed in equation (6) and Figure 11.) Predictions of the continuum model are clearly superior to those of the point mass model, especially during the most rapid avalanche motion (from ~0.2 to 0.6 s in Figure 11). The distinction between the predictions of the continuum model and point mass model are greatest for experiment B, wherein multidimensional effects are strongest near the base of the slope. However, given the vast differences in information content and computational sophistication in the two models, the gains in accuracy afforded by the multidimensional continuum model are perhaps more subtle than expected, especially with respect to the timing and distance of runout termination.

[49] The similarities in runout predictions illustrated in Figure 11 serve to illustrate two important points, one physical and one philosophical. The physical point is that the dynamics of the leading edge or front of an avalanche of homogenous Coulomb material differ rather subtly from the dynamics of a Coulomb point mass. Grains at the avalanche front experience relatively weak interactions with other grains. An exception occurs during the earliest stages of avalanche motion, when steep gradients in thickness h are common near the avalanche front and the resulting longitudinal forces drive downslope acceleration that exceeds that of an isolated point mass. Thus point mass motion lags behind that of the experimental avalanches and multidimensional predictions (Figure 11). However, because of a compensating omission in the point mass model (i.e., neglect of centripetal accelerations that increase basal Coulomb friction when masses descend slopes with convex longitudinal profiles), the model predicts runout times and distances that almost match the those of the data and multidimensional predictions. This success of the point mass model is therefore partly fortuitous.

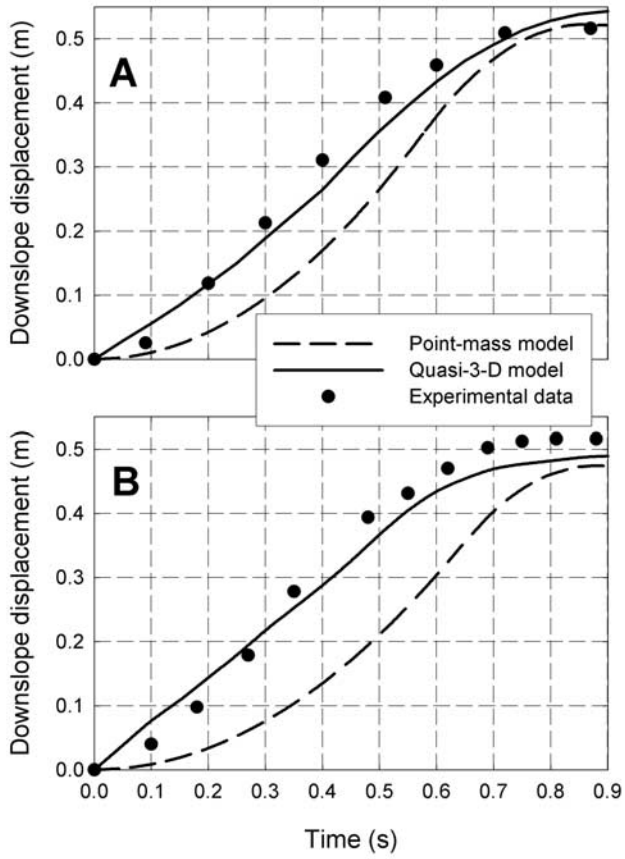

Figure 11. Displacement of avalanche fronts as indicated by data and predicted by our quasi three-dimensional continuum model and a point mass model. All predictions use the friction angles listed in Table 2. (a) Comparisons for experiment A. (b) Comparisons for experiment B.

[50] The apparent success of the point mass model illustrates a key consideration in testing avalanche models with data. Commonly, such models focus almost exclusively on predicting the distal extent of avalanche runout [*Legros*, 2002]. However, as noted by *Feynman* [1994], tests of models against a single type of data or outcome are relatively undemanding and may lead to the spurious conclusion that a model is "correct," even if it is fundamentally flawed. Figure 11 summarizes all possible predictions and tests of the point mass model with our experimental

data, but it depicts only a small fraction of the prediction and testing information available in Figures 9 and 10. Whereas the point mass model predicts exclusively the downslope motion of the avalanche front as a function of time, our multidimensional continuum model predicts this property plus the distributions of downslope and cross-slope displacement and avalanche thickness as functions of x, y, and t. Simultaneous prediction of these multiple interdependent variables affords a much higher standard of testing than is possible when only a single variable is predicted, a principle that has implications in a wide variety of modeling contexts [cf. *Furbish*, 2003].

6. Conclusions

[51] Scaling considerations indicate that miniature experiments can be used to test models of ideal granular avalanches, in which the effects of intergranular fluid and cohesion are negligible. We found that such experiments are particularly useful for testing the ability of a numerical model to predict avalanche motion across complex, three-dimensional terrain. Model testing is enhanced by collection of detailed data on all phases of avalanche motion, rather than on a single aspect of avalanche behavior such as the distal extent of runout. Experimental testing under tightly constrained and monitored conditions is also a crucial step toward model application to geophysical avalanches, which are generally poorly constrained and incompletely characterized and which may involve complicated (and scale-dependent) effects of intergranular fluid and cohesion.

[52] The most important conclusion derived from our experiments is that a conceptually simple Coulomb continuum model can yield quite accurate predictions of granular avalanche motion across irregular three-dimensional terrain, from initiation to deposition. We attribute this accuracy to the prevalence of Coulomb-like behavior (i.e., proportionality of shear and normal stresses) in deforming granular masses over a wide range of quasi-static and dynamic conditions and to three features of our computational model: (1) a depth-averaged mathematical formulation that accounts for the effects of vertical accelerations and adheres closely to the principles of mass and momentum conservation; (2) the use of a suitable methodology for accurately resolving Coulomb stresses; and (3) the use of an appropriate, high-resolution method for computing solutions of the governing equations. The accuracy of our model predictions indicates that complicated constitutive postulates are unnecessary to explain the dynamics of granular avalanches if no effects of intergranular fluid or cohesion are present.

[53] An ancillary conclusion is that the interplay of basal friction, internal friction, and multidimensional mass and momentum conservation affects the behavior of granular avalanches. Three-dimensional topography influences all of these phenomena in a manner that varies with time and position as avalanche motion proceeds from initiation to deposition. Therefore it is unlikely that topographic influences can be parameterized successfully by a bulk roughness or energy loss coefficient, as is necessary in simplified models that neglect multidimensional momentum conservation [cf. *Hungr*, 1995].

[54] **Acknowledgments.** We thank Joseph Walder, Randall LeVeque, Kolumban Hutter, Garry Clarke, and an anonymous reviewer for thoughtful critiques of the manuscript. We thank Richard LaHusen for designing the electronic timer we used for time stamping the digital photographs.

References

Bagnold, R. A. (1954), Experiments on a gravity-free dispersion of large solid spheres in a Newtonian fluid under shear, *Proc. R. Soc. London, Ser. A*, *225*, 49–63.

Coulomb, C. A. (1776), Sur une application des règles de maximis & minimis à quelques problèms de statique, relatifs à l'architecture, in *Mémoires de Mathématique et de Physique*, *Presented at the Royal Academy of Sciences*, *1773*, pp. 343–384, Imperial R. Acad. Sci., Paris.

Davies, T. R. H., and M. J. McSaveney (1999), Runout of dry granular avalanches, *Can. Geotech. J.*, *36*, 313–320.

Denlinger, R. P., and R. M. Iverson (2001), Flow of variably fluidized granular masses across three-dimensional terrain: 2. Numerical predictions and experimental tests, *J. Geophys. Res.*, *106*, 553–566.

Denlinger R. P., and R. M. Iverson (2004), Granular avalanches across irregular three-dimensional terrain: 1. Theory and computation, *J. Geophys. Res.*, *109*, F01014, doi:10.1029/2003JF000085.

Feynman, R. P. (1994), *The Character of Physical Law*, 167 pp., Mod. Libr., New York.

Furbish, D. J. (2003), Using the dynamically coupled behavior of land-surface geometry and soil thickness in developing and testing hillslope evolution models, in *Prediction in Geomorphology*, *Geophys. Monogr. Ser.*, vol. 135, edited by P. R. Wilcock and R. M. Iverson, pp. 169–181, AGU, Washington, D. C.

Gray, J. M. N. T., M. Wieland, and K. Hutter (1999), Gravity driven free surface flow of granular avalanches over complex basal topography, *Proc. R. Soc. London, Ser. A*, *455*, 1841–1874.

Gray, J. M. N. T., Y.-C. Tai, and S. Noelle (2003), Shock waves, dead zones and particle-free regions in rapid granular free-surface flows, *J. Fluid Mech.*, *491*, 161–181.

Heim, A. (1932), *Bergsturz und Menschenleben*, 218 pp., Fretz and Wasmuth, Zürich, Switzerland.

Hungr, O. (1995), A model for the runout analysis of rapid flow slides, debris flows, and avalanches, *Can. Geotech. J.*, *32*, 610–623.

Hunt, M. L., R. Zenit, C. S. Campbell, and C. E. Brennen (2002), Revisiting the 1954 suspension experiments of R. A. Bagnold, *J. Fluid Mech.*, *452*, 1–24.

Hutter, K., and T. Koch (1991), Motion of a granular avalanche in an exponentially curved chute: Experiments and theoretical predictions, *Philos. Trans. R. Soc. London, Ser. A*, *334*, 93–138.

Iverson, R. M. (1997), The physics of debris flows, *Rev. Geophys.*, *35*, 245–296.

Iverson, R. M. (2003), How should mathematical models of geomorphic processes be judged?, in *Prediction in Geomorphology*, *Geophys. Monogr. Ser.*, vol. 135, edited by P. R. Wilcock and R. M. Iverson, pp. 83–94, AGU, Washington, D. C.

Iverson, R. M., and R. P. Denlinger (2001), Flow of variably fluidized granular masses across three-dimensional terrain: 1. Coulomb mixture theory, *J. Geophys. Res.*, *106*, 537–552.

Iverson, R. M., and J. W. Vallance (2001), New views of granular mass flows, *Geology*, *29*, 115–118.

Legros, F. (2002), The mobility of long-runout landslides, *Eng. Geol.*, *63*, 301–330.

LeVeque, R. J. (2002), *Finite-Volume Methods for Hyperbolic Problems*, Cambridge Univ. Press, New York.

Logan, J. D. (1987), *Applied Mathematics: A Contemporary Approach*, John Wiley, Hoboken, N. J.

Louge, M. Y., and S. C. Keast (2001), On dense granular flows down flat frictional inclines, *Phys. Fluids*, *13*, 1213–1233.

McDonald, R. R., and R. S. Anderson (1996), Constraints on eolian grain flow dynamics through laboratory experiments on sand slopes, *J. Sediment. Res.*, *66*, 642–653.

Mitchell, J. K. (1976), *Fundamentals of Soil Behavior*, John Wiley, Hoboken, N. J.

Pouliquen, O., and Y. Forterre (2002), Friction laws for dense granular flows: Application to the motion of a mass down a rough inclined plane, *J. Fluid Mech.*, *453*, 133–151.

Savage, S. B. (1984), The mechanics of rapid granular flows, *Adv. Appl. Mech.*, *24*, 289–366.

Savage, S. B., and K. Hutter (1989), The motion of a finite mass of granular material down a rough incline, *J. Fluid Mech.*, *199*, 177–215.

Savage, S. B., and K. Hutter (1991), The dynamics of avalanches of granular materials from initiation to runout, part I, Analysis, *Acta Mech.*, *86*, 201–223.

Shreve, R. L. (1968), Leakage and fluidization in air-layer-lubricated avalanches, *Geol. Soc. Am. Bull.*, *79*, 653–658.
Voight, B. (Ed.) (1978), *Rockslides and Avalanches, I. Natural Phenomena*, Elsevier Sci., New York.
Voight, B., R. J. Janda, H. Glicken, and P. M. Douglas (1983), Nature and mechanics of the Mount St. Helens rockslide-avalanche of 18 May 1980, *Geotechnique*, *33*, 243–273.
Vreugdenhil, C. B. (1994), *Numerical Methods for Shallow-Water Flow*, Kluwer Acad., Norwell, Mass.
Wieland, M., J. M. N. T. Gray, and K. Hutter (1999), Channelized free-surface flow of cohesionless granular avalanches in a chute with shallow lateral curvature, *J. Fluid Mech.*, *392*, 73–100.

R. P. Denlinger, R. M. Iverson, and M. Logan, U.S. Geological Survey, 1300 SE Cardinal Court #100, Vancouver, WA 98683, USA. (roger@usgs.gov; riverson@usgs.gov; mlogan@usgs.gov)